High-spatial-resolution measurements of iron isotopes in pyrites by secondary ion mass spectrometry using the new Hyperion-II radio-frequency plasma source

Marie-noëlle Decraene, Johanna Marin-carbonne, Anne-sophie Bouvier, Johan Villeneuve, Nordine Bouden, Béatrice Luais, Etienne Deloule

Decraene Marie Noelle (Orcid ID: 0000-0002-3929-9447)

Villeneuve Johan (Orcid ID: 0000-0002-9892-8530)

High spatial resolution measurements of iron isotopes in pyrites by SIMS using the new Hyperion-II Radio-Frequency Plasma source.

Marie-Noëlle Decraene[1,2*], Johanna Marin-Carbonne[1], Anne-Sophie Bouvier[1], Johan Villeneuve[2], Nordine Bouden[2], Béatrice Luais[2] and Etienne Deloule[2].

[1]Institut des Sciences de la Terre, Université de Lausanne, Lausanne, Suisse.

[2] Université de Lorraine, CNRS, CRPG, F-54000 Nancy, France.

*Corresponding author contact: marie-noelle.decraene@unil.ch

Key words: Iron isotopes; Ion microprobe; Pyrites.

Abbreviations: SIMS: Secondary Ions Mass Spectrometry; MC-ICP-MS: Multi-collector inductively coupled plasma mass spectrometry; IMF: Instrumental Mass Fractionation; SD: Standard Deviation; SE: Standard Error.

This article has been accepted for publication and undergone full peer review but has not been through the copyediting, typesetting, pagination and proofreading process which may lead to differences between this version and the Version of Record. Please cite this article as doi: 10.1002/rcm.8986

Abstract

Rationale: Iron isotopic signatures in pyrites are considered as a good proxy to reconstruct paleoenvironmental and local redox conditions. However, the investigation of micro-pyrites less than 20µm in size has been limited by the evaluable analytical techniques. The development of the new brighter radio-frequency plasma ion source (Hyperion-II source) enhances the spatial resolution by increasing the beam density 10 times compared with the Duoplasmatron source.

Methods: Here we present high spatial resolution measurements of iron isotopes in pyrites using a 3nA-3µm primary $^{16}O^-$ beam on two Cameca IMS 1280-HR2 ion microprobe instruments equipped with Hyperion sources at CRPG-IPNT (France) and at SwissSIMS (Switzerland). We tested analytical effects, such as topography and crystal orientation that could induce analytical biases perceptible through variations of the Instrumental Mass Fractionation (IMF).

Results: The δ^{56}Fe reproducibility for the Balmat pyrite standard is ±0.25‰ (2SD, standard deviation) and the typical individual internal error is ±0.10‰ (2SE, standard error). The sensitivity on $^{56}Fe^+$ was $1.2x10^7$cps/nA/ppm or better. Tests on Balmat pyrites revealed that neither the crystal orientation nor channeling effects seem to significantly influence the IMF. Different pyrite standards (Balmat and SpainCR) were used to test the accuracy of the measurements. Indium mounts must be carefully prepared with sample topography < 2µm, which was checked using an interferometric microscope. Such a topography is negligible for introducing change in the IMF. This new source increases the spatial resolution while maintaining the high precision of analyses and the overall stability of the measurements compared with the previous Duoplasmatron source.

Conclusions: We developed a reliable method to perform accurate and high-resolution measurements of micrometric pyrites. The investigation of sedimentary micro-pyrites will improve our understanding of the processes and environmental conditions during pyrite precipitation, including contribution of primary (microbial activities or abiotic reactions) and secondary signatures (diagenesis and/or hydrothermal fluid circulation).

1. Introduction

Iron stable isotope geochemistry has been developed rapidly over the last 15 years, particularly because iron is a ubiquitous element that occurs in three oxidation states: Fe^0, Fe^{2+} and Fe^{3+}. The redox state affects the iron isotope fractionation of the four stable isotopes, ^{54}Fe (5.80%), ^{56}Fe (91.72%), ^{57}Fe (2.20%) and ^{58}Fe (0.28%), following the mass- and temperature-dependent fractionation laws[1,2,3,4]. The iron isotopic composition is reported using the delta (δ) notation (in ‰) defined as deviations of the measured $^{56}Fe/^{54}Fe$ or $^{57}Fe/^{54}Fe$ ratios of the sample relative to the international standard IRMM-014 ($^{56}Fe/^{54}Fe$ value of 15.6986 and $^{57}Fe/^{54}Fe$=0.3626) [5,6] :

$$\delta^{5x}Fe = \left[\frac{\left(\frac{^{5x}Fe}{^{54}Fe}_{sample} \right)}{\left(\frac{^{5x}Fe}{^{54}Fe}_{IRMM014} \right)} - 1 \right]$$

where x is either 6 or 7. The accuracy and precision were determined by the analysis of in-house pyrite standards, Balmat and SpainCR (detailed in section 2.1).

The difference of Fe isotopic compositions between 2 species defines the isotopic fractionation. Iron isotope systematics is used in numerous fundamental fields, such as cosmochemistry and igneous petrology that focus on the accretion of planetary bodies, magmatic differentiation, and diffusion during crystal growth[5,7,8,9,10,11], as well as in environmental geochemistry for understanding the past and modern redox marine cycle[5,12,13,14,15,16,17]. Iron is also a major element in numerous biological reactions leading to diagnostic isotopic fractionations and, thus, can be a good proxy for biosignature recognition. The microbial iron cycle is controlled by Dissimilatory Iron Reduction (DIR) and bacterial iron oxidation leading to precipitation of diverse Fe(II)-bearing biominerals, including iron sulfides[18,19]. However, pyrites can also be formed through abiotic reactions. Both biological and abiotic pathways are associated with large mass-dependent Fe isotopic fractionations[20 to 33]. Consequently, biologically-precipitated pyrites record $\delta^{56}Fe$ variations up to 6‰[20,22,23,24], encompassing the entire range of terrestrial Fe isotopic fractionation (see e.g., ref. 13, 34 for a review). The formation of sedimentary pyrites is a complex, multi-stage process that includes dissolution of FeS_m precursors such as mackinawite (FeS) or greigite (Fe_2S_3) [e.g. 35,36]. Importantly, biologically-mediated sulfides are typically very small, <1µm in size, as illustrated by FeS precipitates in microbial sulfate reducing bacteria cultures (reviewed in ref. 37). The dissolution of those FeS precursors leads to the precipitation of pyrites ranging from <1 to tens of micrometers in size (especially for

sedimentary pyrite framboids)[38], which induces analytical challenges for isotopic measurements in a single pyrite grain.

Investigation of iron isotope variability started with application of Thermal Ionization Mass Spectrometry (TIMS) and was subsequently followed by Multi Collection Inductively Coupled Plasma Mass Spectrometry (MC-ICPMS) yielding higher sensitivity and higher precision measurements. As a result, the application of MC-ICPMS method on igneous rocks allowed the recognition of small iron isotope variations associated with high temperature fractionation processes[32,8,33]. However, only few studies focused on microscale isotope variations in biogeochemistry. For instance, depending on the technique, strong contrasts in Fe isotope compositions have been documented in pyrites from the 2.7 Ga Tumbiana Formation (Pilbara craton, Western Australia). Bulk rock analyses produced a narrow range of δ^{56}Fe values of -0.02 ±0.26‰ (2SD, standard deviation)[15], while *in situ* analyses by LA-MC-ICPMS (Laser Ablation Multi Collector Inductively Coupled Plasma Mass Spectrometry) yielded a wide range of δ^{56}Fe values, from -2.9‰ to +1.5‰[42,43]. Similarly, in Archean pyrite nodules (2.7 Ga shale from Bubi Greenstone Belt, Zimbabwe), the bulk δ^{56}Fe values were around -1.4‰ whereas *in situ* measurements by Secondary Ion Mass Spectrometry (SIMS) described rim to core profiles from +0.5‰ to -2‰[16]. These two examples strongly support the importance of combining whole rocks and micrometer scale *in situ* analysis to constrain primary and/or secondary signals recorded in a pyrite.

Available on the market since 2015, the new radio-frequency oxygen ion source on SIMS instruments, the Hyperion-II, has the primary beam current density improved 10 times compared with the conventional Duoplasmatron oxygen source[44]. The characteristics of the primary beam and secondary transmission are documented in ref. 44. For a given primary beam intensity, the improved current density increases the spatial resolution while maintaining analytical precision compared with the previous $^{16}O^-$ source performance. The improvement of secondary ion transmission, and higher precision and reproducibility measurements have been reported for Mg[44,45] and Si[46] isotope systems. For example, an external reproducibility of ±0.2‰ (2SD) on Δ^{26}Mg* (independent mass fractionation) is achieved with a primary beam size of 3-4 µm[44], much smaller than the 15 µm achievable with the Duoplasmatron source[47]. The new source has also higher sensitivity per unit area for Pb isotopes with a 10 nA primary beam, allowing the precision of U-Pb dating measurements of zircons to be enhanced[44]. Therefore, one of the main advantages of the Hyperion source is the improved spatial resolution achieved without a loss in the precision required for resolving biogeochemical processes.

Previously, the expected precision of ±0.2‰ (2SD) for iron isotope analysis was obtained with a 10 nA primary intensity beam delivered by the Duoplasmatron, focused into a ~15 µm spot to generate enough secondary ion intensity to be collected by Multi Collection Faraday Cups. However, such spot sizes limited the investigation of Fe isotopes in micrometric grains, whereas the Hyperion source opens new possibilities for the studies of biochemical processes.

In order to explore micrometric scale variations of iron isotope in pyrites, we have adapted a previously described analytical procedure by using the Hyperion source, combining the reduction of the spot size for a given intensity, and maintaining a precision of 0.2‰ (2SD). This protocol has been tested on two different SIMS instruments and will open a new analytical field to study iron isotope microscale variabilities in sedimentary pyrites.

2. Experimental:

SIMS measurements were carried out using the Cameca® IMS 1280-HR2 ion probes at CRPG-IPNT (Nancy, France) and SwissSIMS (University of Lausanne, Switzerland), both equipped with the new Hyperion-II Radio frequency source. We performed four Fe isotope sessions at CRPG-IPNT (February 2018, April 2018, July 2018 and September 2020) and four sessions at SwissSIMS (July 2019, January 2020, March 2020 and June 2020).

2.1.Standards

The stability of both instruments was monitored by running multiple measurements of in-house pyrite standards, either Balmat or SpainCr pyrites, that were also used to correct a possible instrumental drift. The major element composition of Balmat pyrite is described in ref. 48 and contains 46.5wt.% of iron and 53.6wt.% of sulfur. This pyrite standard is extensively used for SIMS Fe and S isotopes analyses[16,48,49,50]. The major and trace element compositions of SpainCR pyrite was determined using a JEOL JXA-8530F electron microprobe at the University of Lausanne and data are available in **supporting information A**. The analytical parameters are described in **supporting information B**. SpainCR pyrite grains contain 46.6wt.% of Fe and 53.1wt.% of S. Co, Mn, Cr, Zn and Cu contents are below the detection limit. Pb, Ti and Ni contents are 1112ppm, 1003ppm and 354ppm, respectively. The SpainCR standard was previously used for SIMS S isotope analysis[50,51]. The iron isotopic composition of SpainCR pyrite was determined at CRPG. Chemistry for Fe purification, and Fe isotopic analysis using the Neptune*Plus* MC-ICP-MS are detailed in ref. 40, 41 and 48. In order to evaluate the homogeneity of Fe isotopic composition of SpainCR pyrite standard, core

and rim separates have been chemically processed and analyzed. The bulk Fe isotope measurement sequence follows the sample/standard bracketing method, with IRMM-014 Fe as the normalizing standard. We obtained similar δ^{56}Fe (and δ^{57}Fe) values of +0.516 ±0.05‰ (+0.804 ±0.03‰) (2SD) and +0.521 ±0.02‰ (+0.795 ±0.01‰) (2SD) for core and rim, respectively, for n= 3 replicates of each. This gives a $\delta^{56}Fe_{mean}$ reference value of 0.52 ±0.03‰ for this highly homogeneous SpainCR pyrite standard. Data accuracy and 2SD reproducibility are evaluated by replicate analyses of geostandards, with values of δ^{56}Fe = +0.648 ±0.129 ‰ and δ^{57}Fe = +0.960 ±0.163‰ (n=3) for IF-G (BIF Greenland), and δ^{56}Fe = +0.098 ±0.033‰ and δ^{57}Fe = +0.143 ±0.057‰ (n=15) for BIR-1 (USGS Iceland basalt) during the course of this study. These values are within the reference values in ref. 5. The homogeneity of SpainCR standard was tested by SIMS by measuring three different grains prepared in the same mount (July 2018 session at CRPG-IPNT). Based on 68 measurements, the external reproducibility was ±0.28‰ (2SD) (**Figure S1, supporting information B**).

As no chromium was detected in the pyrite reference materials, Russie magnetite standard was used to evaluate the degree of ^{54}Cr interference on ^{54}Fe, which was necessary for the natural samples due to the presence of Cr. Details are given below in section 2.5.

2.2.Sample preparation

Standard grains were embedded in epoxy and polished with 0.5µm diamond paste. Those grains were carefully removed from epoxy and pressed into 1-inch indium mount. White light interferometric microscope (Bruker Contour GTK at University of Lausanne) was used to measure the sample topography. The relief across the analyzed surface was below 5µm[52]. Samples were coated with a 35nm thick gold film to ensure the conductivity between the sample surface and the SIMS holder.

2.3. Electron backscatter diffraction (EBSD):

In order to check for the influence of crystallographic orientations on SIMS measurements, three Balmat pyrite grains were removed from the Indium mount, embedded in epoxy resin with the analyzed mineral surfaces facing upwards. To eliminate any residual surface damage, the mount was further polished for 40 min using the combined chemical and mechanical effect of an alkaline (pH=9.8) suspension of colloidal silica (0.05 µm). The sample was not carbon-coated before electron backscatter diffraction (EBSD) analysis in order to maximize the detected signal. The crystallographic orientation patterns were acquired at the

University of Lausanne, Switzerland, using a Tescan Mira II LMU field emission-scanning electron microscope (FE-SEM) equipped with the Symmetry detector and the Aztec 4.2 software package, both released by Oxford Instruments®. Acquisition parameters included an acceleration voltage of 20 kV, a probe current of 1.1 nA, a working distance of 23 mm, and a 70° tilt of the sample surface with respect to the horizontal. As pyrite has a cubic crystal structure, [100], [010], and [001] axes are equivalent and orthogonal, and the maximum misorientation imposed by symmetry is 62.8°. The pyrite (m3)[53] match unit (a = 5.4166Å) was used as a reference file for the indexing of the EBSD patterns, the high quality of which was attested by a mean angular deviation (MAD) value ranging between 0.2 and 0.6. Six to ten EBSD patterns per grain were collected and the average crystallographic orientations represented in an upper hemisphere equal area pole figure of Euler angle triplets (φ_1,Φ,φ_2). For more information on the basics of the EBSD technique, the reader is referred to e.g. ref. 54.

2.4.SIMS settings:

Samples were stored in the vacuum chamber at $2.5x10^{-8}$ mbar to $2x10^{-9}$ mbar. Samples were sputtered with a 3nA $^{16}O^-$ primary beam accelerated by a 13kV high voltage. The corresponding spot size was 2.5µm to 3µm (**Figure 2**). The primary beam was mainly focused through L3 and L4 lenses of the primary column in Gaussian mode and the aberration was reduced by using a PBMF aperture of 200µm. The L4 aperture was maintained open at 750µm. These settings of primary beam apertures were the same for both instruments and the main SIMS settings are summarized in **Table 1**. The entrance slit was set to 61µm at SwissSIMS and 85µm at CRPG-IPNT, corresponding to a MRP (for Mass Resolving Power) of M/ΔM~ 6700-7000 (slit 3) at SwissSIMS and M/ΔM~ 6100 (slit 3) at CRPG-IPNT resolving the interference of $^{53}CrH^+$ on $^{54}Fe^+$ (M/ΔM= 6088). The interference of $^{54}Cr^+$ on $^{54}Fe^+$ (MRP~74,000) was monitored by analyzing $^{52}Cr^+$ as described in ref. 48. Although pyrite standards have no detectable Cr, hundreds to a thousand of counts of ^{52}Cr are measured in natural pyrites, calling for a need to estimate the $^{54}Cr^+$ contribution at mass 54 and then correct for it. The correction scheme for Cr was established using a magnetite standard, which has a detectable amount of Cr, resulting in a final correction of ~0.15‰ on $\delta^{56}Fe$ per $1x10^4$ counts per second (cps) of $^{52}Cr^+$. The interference of $^{56}FeH^+$ on $^{57}Fe^+$, which requires a MRP of 7700 could not be clearly resolved with the chosen slit settings. However, this high spatial resolution method is developed in order to analyze $\delta^{56}Fe$ values in micrometric pyrites. To obtain a maximum internal error of 0.3‰ (2SE standard error) on $\delta^{56}Fe$, the minimum $^{56}Fe^+$ intensity

on the pyrite standard should be $4x10^7$cps, which cannot be attained under MRP>7000. Pyrite being nominally anhydrous mineral held under the chamber vacuum of ~$2x10^{-9}$ mbar yields low interferences of $^{56}FeH^+$ with the $^{57}Fe^+$. When pyrites are prepared in an indium mount, the iron hydride was not detected on the faraday cup (FC) measurements (see section 2.5). The secondary ion beam was filtered by an energy slit of 50 eV. A 2000µm square field aperture was used to clip ~10% of the signal and to remove off-axis aberrations of the secondary ion beam. We used a transmission setting (Maximum Area 80) leading to a field of view of the sample of 20x20µm in the field aperture. The secondary $^{54}Fe^+$, $^{56}Fe^+$, $^{57}Fe^+$ and $^{52}Cr^+$ ions were accelerated at 10kV and analyzed on three off-axis FCs and one electron multiplier (EM) (detectors C, H1, H'2 and L2 respectively). The C and H1 FCs were equipped with $10^{11}\Omega$ resistors. The H'2 FC was equipped with a $10^{12}\Omega$ resistor at CRPG-IPNT and a $10^{11}\Omega$ resistor at SwissSIMS. The relative yields of the amplifiers of the FCs were calibrated before each session on both ion microprobes and the background noises of the FCs were measured for each analysis. The high voltage of the EM (EM HV) was adjusted before each session. No aging effect of the EM was observed during the session. Presputtering time is necessary to remove the 35nm of gold and potential surface contamination, to implant primary ions in the sample surface and to get a stable secondary signal. The intensity of $^{56}Fe^+$ increased until it became stable after 90s (**Figure S2, supporting information B**). The intensity of the signal is then stable with a typical count rate between $4x10^7$ and $5x10^7$cps when using a 3nA primary beam intensity.

The analytical routine then consisted of 90s of presputtering followed by 60 cycles (5s each) of collection separated by 0.08s waiting time, for a total of 7 min per analysis. After presputtering, automatic beam centering in the field and contrast apertures, the energy slit and transfer deflectors were performed routinely. The typical count rate of $^{54}Fe^+$, $^{56}Fe^+$ and $^{57}Fe^+$ are $3.2x10^6$, $4.8x10^7$ and $1.1x10^6$cps respectively for Balmat reference material measured at the SwissSIMS instrument tuned with a primary beam intensity of 3.05nA and $4.3x10^6$, $6.4x10^7$ and $1.4x10^6$cps, respectively, at the CRPG-IPNT instrument tuned with a primary beam intensity ranging from 3.2 to 3.5nA (**Table 1**). The difference in ion counting intensities between the two instruments is due to the higher primary current set at CRPG-IPNT and also reflects a differential transmission due to the use of a larger entrance slit at CRPG-IPNT. The internal precision on $\delta^{56}Fe$ of Balmat standard was ±0.10‰ (2SE). The reproducibility is reported in terms of 2SD, standard deviation. The external reproducibility ranges between

±0.24‰ (n=33) to ±0.30‰ (n=17, 2SD) at CRPG-IPNT and from ±0.15‰(n=10) to ±0.28‰ (n=39, 2SD) at SwissSIMS (**Table 2**).

2.5.Mass Interferences ($^{53}CrH^+$ and $^{56}FeH^+$):

The required MRP to resolve the isobaric interference of $^{54}Cr^+$ on $^{54}Fe^+$ is out of the ion microprobe capabilities (MRP~74,000), thus, the interference was indirectly quantified by measuring $^{52}Cr^+$. The detailed procedure for Cr correction[48] shows that the $^{53}Cr/^{52}Cr$ ratio measured by SIMS is similar to that determined from Cr isotopes natural abundances (^{52}Cr=83.8%, ^{53}Cr=9.5% and ^{54}Cr=2.4%). We thus used the natural abundances of Cr isotopes combined with the measured $^{52}Cr^+$ intensity to calculate the $^{54}Cr^+$ intensity in standards and samples and then corrected the ^{54}Cr contribution from the measured ^{54}Fe signal. The $^{53}CrH^+$ peak height was measured in Russie magnetite standard, on the axial EM (monocollection mode), using a 800pA primary beam intensity to obtain ~$2x10^5$cps on $^{54}Fe^+$ and to not saturate the detector. Under a vacuum of $3.4x10^{-9}$mbar, $^{53}CrH^+$ peak represents less than 0.05% of the $^{54}Fe^+$ peak (**Figure 1A**). Tens of counts are detected for $^{52}Cr^+$ in pyrite standards using a 3nA primary beam, meaning that this hydride contribution can be ignored.

Accuracy of analysis can also be impacted by the interference of $^{56}FeH^+$ on $^{57}Fe^+$. In this study, the MRP was set lower (~6800) than that required to separate these two species. Getting a higher MRP to have accurate $\delta^{57}Fe$ data would decrease the precision of $^{56}Fe/^{54}Fe$ ratios. However, the contribution from $^{56}FeH^+$ hydride has been measured to evaluate the reliability of $^{57}Fe/^{54}Fe$ ratios. High resolution scan (MRP 7800) of the mass ^{57}Fe was carried out on the axial EM using a 1nA primary beam intensity (**Figure 1C**). The magnitude of $^{56}FeH^+$ peak is 0.05% of the $^{57}Fe^+$ peak height due to good vacuum conditions in the analysis chamber (~$3.4x10^{-9}$mbar) but can be up to 0.2% of the $^{57}Fe^+$ peak height when vacuum conditions deteriorate to $2x10^{-8}$mbar. The level of $^{56}FeH^+$ formation is thus estimated to 0.01‰-0.04‰. At MRP 6800, the mass scan shows that ^{57}Fe flat top is affected by the tail of the hydride peak (**Figure 1B**). The hydride contribution on ^{57}Fe signal is thus insignificant for measurements done in indium mounts. The contribution of hydrides to the Fe isotopic signal, in particular the interference of $^{56}FeH^+$ with $^{57}Fe^+$, can also be evaluated by the relationship between the $^{56}Fe/^{54}Fe$ and $^{57}Fe/^{54}Fe$ ratios. Pyrites from sedimentary rocks (Sonoma basin, USA) and standards (Balmat pyrite) measured during the July 2020 session are plotted in a three-isotopes diagram using the natural logarithm of the measured $^{56}Fe/^{54}Fe$ and $^{57}Fe/^{54}Fe$ ratios (**Figure 1D,** data available in **Table S1, supporting information B**). All the data define a slope of 0.679

(±0.007) with a correlation coefficient r^2 of 0.987, which is consistent with the expected mass-dependent fractionation slope of 0.678. Since the measured slope is consistent with the terrestrial mass fractionation slope, the contribution of $^{56}FeH^+$ to the $^{57}Fe/^{54}Fe$ ratio is assumed negligible. Sample mounting using indium rather than epoxy together with vacuum conditions below $5x10^{-9}$mbar are crucial for maintaining small hydride contributions and to produce reliable $\delta^{57}Fe$ data and high precision $\delta^{56}Fe$ values.

2.6. IMF correction:

The effect of a mass dependent fractionation due to the instrument (IMF for Instrumental Mass Fractionation) is defined as:

$\alpha_{inst} = \frac{\left(\frac{^{56}Fe}{^{54}Fe}\right)_{measured}}{\left(\frac{^{56}Fe}{^{54}Fe}\right)_{true}}$ or $\Delta^{56}Fe\ inst\ (‰) = \delta^{56}Fe\ measured - \delta^{56}Fe\ true$ by using the approximation $\Delta^{56}Fe_{inst} \approx \ln(\alpha_{inst})$.

The "measured" and "true" $\delta^{56}Fe$ values are iron isotopic composition measured in the same reference material by SIMS and MC-ICP-MS. The typical IMF on pyrite is ~ -30 ±5‰, measured by both Hyperion-II and Duoplasmatron sources but the exact value depends on the instrument tuning. For example, a 4‰ shift in the IMF for Balmat pyrite was measured after retuning of the primary beam. Slight modifications of the primary beam (i.e. different high voltages on the primary lenses resulting in similar primary intensity but different beam densities) and entrance slit settings lead to the variation of the IMF on Balmat pyrite between -31.20 and -33.10‰ at CRPG-IPNT and highly variable, from -27.23 to -35.16‰ at SwissSIMS (**Table 2**). We measured the IMF using Balmat pyrite standard to monitor the stability of the ion probe during each session.

3. Results and discussion

3.1. Spot size:

The resolution of ion images of a silicon grid on an electron multiplier is used to estimate the $^{16}O^-$ primary beam size. To find the best possible resolution of the image, (i.e., getting the smallest beam) we tested different combinations of primary lenses, and the best result was obtained by setting the voltage on L1 and L2 to 9800V and 9900V, respectively, and keeping the L3 close to 8500V. The results of the $^{30}Si^+$ ion images are reported in **Figure 2A**. Using a 3nA $^{16}O^-$ beam, the ability to differentiate two silicon bars on the 3µm grid indicates a

spot comparable to 3µm size. The 2µm gap between the two horizontal Si bars is not completely resolved whereas the vertical bars are clearly visible, meaning the spot size is between 2.5 and 3µm. The spot size was verified with a scanning electron microscope (SEM) (**Figure 2B)** and an interferometric microscope (**Figure 2C**) after the SIMS measurements of a sedimentary micro-pyrite and the pyrite standard (Balmat). White light interferometric microscopy allows for the precise quantification of the beam size, by imaging the relief of the beam crater in both X and Y directions (**Figures 2C and 2D**). The primary beam size is measured at the bottom of the pit and corresponds to a ~3µm diameter spot. This quantitative analysis is consistent with the beam size estimated through ion imaging of the Si grid. The sputtered area is extended over a diameter of 6 x 7-9µm depending on the session and the pit is ~3µm deep (**Figure 2D)**. The asymmetric shape of the crater and the larger sputtered area compared to the real primary beam size are due to the incidence angle of the beam with the sample surface, which is characteristic of the Cameca® ion probes (except NanoSIMS) (**Figure 2B**).

3.2.Crystal orientation and topography effects on instrumental mass fractionation (IMF):

The IMF is the main limitation in the accuracy of SIMS analysis[55,56]. It results from various processes occurring during secondary atom ionization, extraction, secondary ion transmission and detection[56]. The IMF is known to be greatly dependent on the sample characteristic (mineralogy, chemical composition and crystallographic orientation[e.g.56,57,58]). This effect is corrected by measuring reference material (same mineral, crystallography and major element chemical compositions) and samples in the same analytical conditions. The IMF variations occur in various isotopic systems, for example, the $\delta^{18}O$ measurements of garnets are strongly affected by their Ca-Fe-Mg content[59,60], as well as $\delta^{34}S$ in Fe-Ni sulfides[57,61,62], and Mg and Si isotopes in silicates (e.g. olivine, glass, pyroxene) with an IMF depending on their Mg content[46,63]. Crystal orientation may also have in some cases a strong influence on the IMF, as demonstrated for example on Fe isotopic compositions in magnetite[58], on S isotope compositions in sphalerite and galena[64] and on U-Pb dating in baddeleyite[65].

As pyrites are not affected by major element substitution, *i.e.* no solid solution or chemical variability, the potential variations of the IMF can only be the result of the crystal orientation and/or the topography. The EBSD pole figure shown in **Figure 3B** displays the crystallographic orientations of the three different grains of Balmat standard projected on a

plane (XY) parallel to the surfaces analyzed by SIMS (and EBSD). With misorientation angles between [100] axes in Grain 1, 2, and 3 (G1-G3) and the reference direction Z (i.e. the normal to the page pointing towards the reader) of 14°, 6°, and 1°, respectively, the analyzed surfaces can be considered nearly parallel to the face of the pyrite unit cell (i.e. normal to the [100] axis). The misorientation angle between the [100] axes located in the middle of the pole figure is 18° between G1 and G2, and 15° between G1 and G3. Fe isotopic measurements show respective mean δ^{56}Fe values and external reproducibility of -0.29 ±0.30‰ (2SD) / ±0.13‰ (2SE, n=5), -0.59 ±0.42‰ (2SD) / ±0.19‰ (2SE, n=5) and -0.32 ±0.44‰ (2SD) / ±0.20‰ (2SE, n=5), for G1, G2, and G3 (**Figure 3A**). Those δ^{56}Fe values suggest that the inter-grain variability is lower than the reproducibility (2SD) and the uncertainty on the averages (2SE). Even though the EBSD measurements on a sample set of only three grains have no statistical significance, it can be said at this stage that no obvious relationship between the crystallographic orientation of pyrite and SIMS δ^{56}Fe measurements has been observed. A thorough review (beyond the scope of this study) based on a wide range of crystallographic orientations is needed to confirm this initial statement. Our results are also consistent with the absence of crystal orientation effects on S isotopes[58,66].

The channeling effect of the primary ion beam as a function of atomic planes orientation has been shown to influence the secondary ion yields and thus the instrumental mass fractionation[67,68]. Similarly to magnetite that exhibits channeling effects and plane-specific IMF for Fe and O isotopes[58], pyrites are cubic minerals that could experience similar effects. This effect was evaluated by rotating the mount in the sample holder by 90°, 180° and 270°. We ran 3 to 6 analyses per rotation (**Table S2, supporting information B**). The mean IMF-corrected $\delta^{56}Fe_{IRMM014}$ values for P0, P1, P2 and P3 are -0.38 ±0.31‰ (2SD) / ±0.13‰ (2SE, n=6) for P0, -0.49 ±0.37‰ (2SD) / ±0.21‰ (2SE, n=3) for P1, -0.38 ±0.12‰ (2SD) / ±0.07‰ (2SE, n=3) for P2 and -0.39 ±0.36‰ (2SD) / ±0.16‰ (2SE, n=5) (**Figure 4**). Considering the external reproducibility (2SD) and the internal error (2SE) together, those data show a similar mean δ^{56}Fe values across the four positions in the holder.

Surface topography could also induce artificial iron isotopic variations, especially when pyrite grains are just slightly bigger than the primary spot size. Here, a core to rim profile on Balmat pyrites was performed in order to examine the edge effect on the reliability of δ^{56}Fe analyses. Fe isotope analyses show similar δ^{56}Fe values between the core and the rim of $\delta^{56}Fe_{BalmatPf1@01}$= -0.27 ±0.11‰ (2SE, n=1, core) and $\delta^{56}Fe_{BalmatPf1@8}$= -0.28 ±0.12‰ (2SE, n=1, rim) and an external reproducibility of ±0.18‰ (2SD) (**Figure 5D,** data available in **Table**

S2 supporting information B). This profile (Pf1) is characterized by a topographic difference of 1.7µm (**Figure 5C**), which is not significant to introduce a bias. However, the last analysis is located at ~20µm from the grain edge that is ~7µm above the enclosing indium. Thus, this value was measured in the slightly tilted shade zone on the edge of the pyrite (**Figure 5A and Figure 5B**), demonstrating the reliability of δ^{56}Fe values.

3.3. Sensitivity:

Sensitivity depends on the sputtering time, ionization, extraction of the Fe^+ ion from the matrix and secondary ions transmission until the detectors. It is defined as count rate per ppm of Fe in the analyzed phase per nA of the primary beam (cps/ppm/nA). As the Fe content is constant in pyrites, the expression of the sensitivity is approximately proportional to the ion yield:

^{56}Fe yield = $^{56}Fe^+$ / P intensity.

The sensitivity calculation is commonly used to evaluate the transmission of an ion microprobe. **Table 1** shows the $^{56+}$Fe ion yields on Balmat pyrite, obtained over the different sessions at CRPG-IPNT and SwissSIMS equipped with the Hyperion-II source. We compared these results to the sensitivity obtained with the conventional Duoplasmatron source from ref. 48 and ref. 49. Sensitivities determined on Balmat pyrite range from $1.56x10^7$ to $2.01x10^7$cps/nA at CRPG-IPNT. Sessions performed at SwissSIMS (July 2019, January 2020, March 2020 and September 2020) show similar sensitivities, ranging from $1.49x10^7$cps/nA to $1.61x10^7$cps/nA. Higher sensitivities obtained at CRPG-IPNT compared to SwissSIMS are explained by different widths of the entrance slit. Sensitivities obtained with the Duoplasmatron source vary from $1.2x10^7$cps/nA (ref. 48) to $1.5x10^7$cps/nA (ref. 49). However, the resulted transmission in the two Duoplasmatron-based studied are not directly comparable as the width of the field aperture (FA), the entrance and exit slit and the Maximum Area (MA) are different between these two studies (**Table 1**). In order to compare sensitivities obtained by Hyperion and Duoplasmatron, we performed two tests using 1) a MA 80 and field aperture closed at ~2500µm (comparable with sensitivity obtained in ref. 48) and 2) a MA 160 and an opened field aperture to transmit 100% of the signal, as in ref. 49. Using a MA of 80 and similar FA, entrance and exit slit widths, the ^{56}Fe sensitivity is $1.56x10^7$cps/nA and better than the $1.2x10^7$cps/nA obtained with the Duoplasmatron (ref.48). The higher sensitivity with the Hyperion is due to the use of a smaller beam, which is less clipped in the field aperture compared to the Duoplasmatron beam. Using a MA 160, we obtained a sensitivity of

$5.05x10^6$cps/nA, which is lower than the $1.5x10^7$cps/nA achieved by the Duoplasmatron[49]. However, these sensitivities are not directly comparable as O_2^- and O^-primary beams were respectively used in ref. 49 and in the present study. The higher sensitivity obtained in ref. 49 can be thus attributed to the more efficient sputtering rate of the O_2^- beam. The use of smaller primary beam currents reduces the size of the crossover and off-axis aberrations of the secondary ion beam, which helps to define a sharper slit image. Therefore, for a given MRP, the entrance slit can be more opened using the Hyperion and this results in a gain of sensitivity compared to the Duoplasmatron. This test illustrates the ability of the source to provide enough secondary ion signals with a 3nA beam focused on a 3µm spot and to achieve a better sensitivity than that delivered by Duoplasmatron. The Fe secondary ion signals produced by the 3nA primary beam can be detected by Multi Collection Faraday Cups and thus, provide high precision δ^{56}Fe measurements along with higher spatial resolution.

3.4.Reproducibility and accuracy:

The reproducibility of the δ^{56}Fe measurements on the Balmat reference material was established over three sessions (February 2018, April 2018 and September 2020) at CRPG-IPNT and four sessions (July 2019, January 2020, March 2020 and June 2020) at SwissSIMS Lausanne (**Table 2**). Balmat pyrite (same grain) displays a long-term reproducibility of ±0.25‰ (2SD) for 166 measurements (**Figure 6**) at CRPG-IPNT and ±0.22‰ (2SD) for 185 measurements (June 2020) at the SwissSIMS ion probe facility. The short-term reproducibility on Balmat pyrite varied from ±0.24‰ (2SD, February 2018, n=33, **Table S3 supporting information B**) to ±0.26‰ (2SD, April 2018, n=133) at CRPG-IPNT and from ±0.18‰ (2SD, March 2020, n=33) to ±0.35‰ (2SD, January 2020, n=16) at SwissSIMS. The reproducibility obtained on the SpainCR standard (July 2018) is close to that measured in Balmat pyrite with a value of ±0.28‰ (2SD, n=61). Published data obtained using the $^{16}O^-$ Duoplasmatron source[69] on three days of analysis show a reproducibility of ±0.44‰ (2SD, n=17) on the same grain of Balmat, which highlights the better stability of the Hyperion-II source than the Duoplasmatron.

The accuracy of the SIMS technique was tested on two pyrite standards which have different isotopic compositions. We used Balmat as a reference standard and considered SpainCR as an unknown pyrite. The δ^{56}Fe value for SpainCR was determined using the IMF calculated on the Balmat reference material. The δ^{56}Fe value for SpainCR pyrite calculated at

+0.64 ±0.26‰ (2SD, n=2) is in quite good agreement with the value of $\delta^{56}Fe$= +0.52 ±0.03‰ determined by MC-ICP-MS, demonstrating the accuracy of the SIMS method.

4. Conclusions:

An ion microprobe equipped with the new Hyperion-II Radio Frequency source is able to determine iron isotope ratios with high accuracy, at high precision (~0.25‰, 2SD) and high spatial resolution (3µm). We have detailed a procedure to achieve $\delta^{56}Fe$ measurements with a primary intensity 3 times lower than that traditionally delivered by the Duoplasmatron source, yet we achieved better precision. The MRP was intentionally set at a lower value than that required to resolve $^{56}FeH^+$ from $^{57}Fe^+$ to attain a minimum $^{56}Fe^+$ count rate of $4x10^7$cps on a pyrite reference material to produce high precision $\delta^{56}Fe$ values. The level of $^{56}FeH^+$ is low compared with the intensity of $^{57}Fe^+$ under high vacuum. An MRP of ~6700 is sufficient to limit its contribution to the ^{57}Fe signal. In our sample set, we demonstrated the absence of topography and crystal orientation effects. Currently, this new procedure is being applied to major iron-bearing minerals to better constrain natural iron isotopic variabilities at micrometric scale in sedimentary pyrites. The future investigation of *in situ* $\delta^{56}Fe$ signatures in minor iron-bearing phases such as oxides, carbonates and silicates will serve as a promising tool to answer fundamental questions in extraterrestrial and terrestrial petrology and to gain a better understanding of the biogeochemical iron cycles.

Acknowledgements:

We thank Caroline de Meyer for assistance with the EBSE analysis. We thank Claire Rollion-Bard for providing SpainCR pyrite standard, Katharina Marger for her help with the EPMA analysis, and Damien Cividini (CRPG) for help in MC-ICP-MS measurements. We thank David Zakharov for fruitful discussions that led to the improvement of the manuscript. We appreciated constructive reviews from Cees-Jan De Hoog and three anonymous reviewers. This research was supported by the European Union's Horizon H2020 research and innovation program ERC (STROMATA, grant agreement 759289; PI Johanna Marin-Carbonne).

References:

1. Beard BL, Johnson CM. High precision iron isotope measurements of terrestrial and lunar materials. *Geochim Cosmochim Acta*. 1999;63(11-12):1653-1660. https://doi.org/10.1016/S0016-7037(99)00089-7.
2. Anbar AD, Roe JE, Barling J, Nealson KH. Nonbiological fractionation of iron isotopes. *Science*. 2000;288(5463):126-128. doi: 10.1126/science.288.5463.126.
3. Dauphas N, Janney PE, Mendybaev RA, et al. Chromatographic separation and multicollection-ICPMS analysis of iron. Investigating mass-dependent and-independent isotope effects. *Anal Chem*. 2004;76(19):5855-5863. https://doi.org/10.1021/ac0497095.
4. Berglund M, Wieser ME. Isotopic compositions of the elements 2009 (IUPAC Technical Report). *Pure Appl Chem*. 2011;83(2):397-410. https://doi.org/10.1351/PAC-REP-10-06-02.
5. Craddock PR, Dauphas N. Iron isotopic compositions of geological reference materials and chondrites. *Geostand Geoanal Res*. 2011;35(1):101-123. https://doi.org/10.1111/j.1751-908X.2010.00085.x.
6. Taylor PDP, Maeck R, De Bièvre P. Determination of the absolute isotopic composition and atomic weight of a reference sample of natural iron. *Int J Mass Spectrom Ion Processes*. 1992; 121(1-2), 111-125.
7. Mullane E, Russell SS, Gounelle M. Nebular and asteroidal modification of the iron isotope composition of chondritic components. *Earth Planet Sci Lett*. 2005;239(3-4):203-218. https://doi.org/10.1016/j.epsl.2005.07.026.
8. Poitrasson F, Freydier R. Heavy iron isotope composition of granites determined by high resolution MC-ICP-MS. *Chem Geol*. 2005;222(1-2):132-147. https://doi.org/10.1016/j.chemgeo.2005.07.005.
9. Needham AW, Porcelli D, Russell SS. An Fe isotope study of ordinary chondrites. *Geochim Cosmochim Acta*. 2009;73(24):7399-7413. https://doi.org/10.1016/j.gca.2009.08.034.
10. Hezel DC, Needham AW, Armytage R, et al. A nebula setting as the origin for bulk chondrule Fe isotope variations in CV chondrites. *Earth Planet Sci Lett*. 2010;296(3-4):423-433. https://doi.org/10.1016/j.epsl.2010.05.029.
11. Dauphas N, John SG, Rouxel OJ. Iron isotope systematics. *Rev Mineral Geochem*. 2017;82(1):415-510. https://doi.org/10.2138/rmg.2017.82.11.
12. Rouxel OJ, Bekker A, Edwards KJ. Iron isotope constraints on the Archean and Paleoproterozoic ocean redox state. *Science*. 2005;307(5712):1088-1091. doi: 10.1126/science.1105692.
13. Johnson CM, Beard BL, Roden EE. The iron isotope fingerprints of redox and biogeochemical cycling in modern and ancient Earth. *Annu Rev Earth Planet Sci*. 2008;36:457-493. doi:10.1146/annurev.earth.36.031207.124139.
14. Severmann S, Lyons TW, Anbar A, McManus J, Gordon G. Modern iron isotope perspective on the benthic iron shuttle and the redox evolution of ancient oceans. *Geology*. 2008;36(6):487-490. https://doi.org/10.1130/G24670A.1.

15. Czaja AD, Johnson CM, Beard BL, Eigenbrode JL, Freeman KH, Yamaguchi KE. Iron and carbon isotope evidence for ecosystem and environmental diversity in the~ 2.7 to 2.5 Ga Hamersley Province, Western Australia. *Earth Planet Sci Lett*. 2010;292(1-2):170-180. https://doi.org/10.1016/j.epsl.2010.01.032
16. Marin-Carbonne J, Rollion-Bard C, Bekker A, et al. Coupled Fe and S isotope variations in pyrite nodules from Archean shale. *Earth Planet Sci Lett*. 2014;392:67-79. https://doi.org/10.1016/j.epsl.2014.02.009.
17. Johnson C, Beard B, Weyer S. *Iron Geochemistry: An Isotopic Perspective.* 2020; Springer, Cham.
18. Johnson CM, Beard B, Roden EE, Newman DK, Nealson KH. Isotopic constraints on biogeochemical cycling of Fe. *Rev Mineral Geochem*. 2004; 55, 359-408. https://doi.org/10.2138/gsrmg.55.1.359
19. Lovley DR, Stolz JF, Nord GL, Phillips EJ. Anaerobic production of magnetite by a dissimilatory iron-reducing microorganism. *Nature*. 1987; 330, 252-254.
20. Bullen TD, McMahon PM. Using stable Fe isotopes to assess microbially-mediated Fe3+ reduction in a jet-fuel contaminated aquifer. *Mineral Mag*. 1998;62:255-256.
21. Beard BL, Johnson CM, Cox L, Sun H, Nealson KH, Aguilar C. Iron isotope biosignatures. *Science*. 1999;285(5435):1889-1892. doi: 10.1126/science.285.5435.1889.
22. Crosby HA, Johnson CM, Roden EE, Beard BL. Coupled Fe (II)− Fe (III) electron and atom exchange as a mechanism for Fe isotope fractionation during dissimilatory iron oxide reduction. *Environ Sci Technol*. 2005;39(17):6698-6704. https://doi.org/10.1021/es0505346.
23. Crosby HA, Roden EE, Johnson CM, Beard BL. The mechanisms of iron isotope fractionation produced during dissimilatory Fe (III) reduction by Shewanella putrefaciens and Geobacter sulfurreducens. *Geobiology*. 2007;5(2):169-189. https://doi.org/10.1111/j.1472-4669.2007.00103.x.
24. Percak-Dennett EM, Beard BL, Xu H, Konishi H, Johnson CM, Roden EE. Iron isotope fractionation during microbial dissimilatory iron oxide reduction in simulated Archaean seawater. *Geobiology*. 2011;9(3):205-220. https://doi.org/10.1111/j.1472-4669.2011.00277.x.
25. Johnson CM, Skulan JL, Beard BL, Sun H, Nealson KH, Braterman PS. Isotopic fractionation between Fe (III) and Fe (II) in aqueous solutions. *Earth Planet Sci Lett*. 2002;195(1-2):141-153. https://doi.org/10.1016/S0012-821X(01)00581-7.
26. Welch SA, Beard BL, Johnson CM, Braterman PS. Kinetic and equilibrium Fe isotope fractionation between aqueous Fe (II) and Fe (III). *Geochim Cosmochim Acta*. 2003;67(22):4231-4250. https://doi.org/10.1016/S0016-7037(03)00266-7.
27. Skulan JL, Beard BL, Johnson CM. Kinetic and equilibrium Fe isotope fractionation between aqueous Fe (III) and hematite. *Geochim Cosmochim Acta*. 2002;66(17):2995-3015. https://doi.org/10.1016/S0016-7037(02)00902-X.
28. Beard BL, Handler RM, Scherer MM, et al. Iron isotope fractionation between aqueous ferrous iron and goethite. *Earth Planet Sci Lett.* 2010;295(1-2):241-250. https://doi.org/10.1016/j.epsl.2010.04.006.

29. Wu L, Beard BL, Roden EE, Kennedy CB, Johnson CM. Stable Fe isotope fractionations produced by aqueous Fe (II)-hematite surface interactions. *Geochim Cosmochim Acta*. 2010;74(15):4249-4265. https://doi.org/10.1016/j.gca.2010.04.060.
30. Wu L, Beard BL, Roden EE, Johnson CM. Stable iron isotope fractionation between aqueous Fe (II) and hydrous ferric oxide. *Environ Sci Technol*. 2011;45(5):1847-1852. https://doi.org/10.1021/es103171x.
31. Frierdich AJ, Nebel O, Beard BL, Johnson CM. Iron isotope exchange and fractionation between hematite (α-Fe2O3) and aqueous Fe (II): A combined three-isotope and reversal-approach to equilibrium study. *Geochim Cosmochim* Acta. 2019;245:207-221. https://doi.org/10.1016/j.gca.2018.10.033.
32. Croal LR, Johnson CM, Beard BL, Newman DK. Iron isotope fractionation by Fe (II)-oxidizing photoautotrophic bacteria. *Geochim Cosmochim Acta*. 2004;68(6):1227-1242. https://doi.org/10.1016/j.gca.2003.09.011.
33. Bullen TD, White AF, Childs CW, Vivit DV, Schulz MS. Demonstration of significant abiotic iron isotope fractionation in nature. *Geology*. 2001;29(8):699-702. https://doi.org/10.1130/0091-7613(2001)029<0699:DOSAII>2.0.CO;2.
34. Beard BL, Johnson CM. Fe isotope variations in the modern and ancient earth and other planetary bodies. *Rev Mineral Geochem*. 2004;55(1):319-357. https://doi.org/10.2138/gsrmg.55.1.319.
35. Rickard D, Grimes S, Butler I, Oldroyd A, Davies KL. Botanical constraints on pyrite formation. *Chem. Geol.* 2007;236: 228-246. https://doi.org/10.1016/j.chemgeo.2006.09.011.
36. Luther III GW. Pyrite synthesis via polysulfide compounds. *Geochim Cosmochim Acta*. 1991;55, 2839-2849. https://doi.org/10.1016/0016-7037(91)90449-F.
37. Rickard D. *Sulfidic sediments and sedimentary rocks*. Newnes. 2017.
38. Rickard D. Sedimentary pyrite framboid size-frequency distributions: A meta-analysis. *Palaeogeo Palaeoclim Palaeoeco*. 2019;522:62-75. https://doi.org/10.1016/j.palaeo.2019.03.010.
39. Teng FZ, Dauphas N, Helz RT, Gao S, Huang S. Diffusion-driven magnesium and iron isotope fractionation in Hawaiian olivine. *Earth Planet Sci Lett*. 2011;308(3-4):317-324. https://doi.org/10.1016/j.epsl.2011.06.003.
40. El Korh A, Luais B, Deloule E, Cividini D. Iron isotope fractionation in subduction-related high-pressure metabasites (Ile de Groix, France). *Contributions to Mineralogy and Petrology*. 2017;172(6):41. doi: 10.1007/s00410-017-1357-x.
41. Liu PP, Zhou MF, Luais B, Cividini D, Rollion-Bard C. Disequilibrium Fe isotope fractionation during the high-temperature magmatic differentiation of the Baima Fe-Ti oxide-bearing mafic intrusion, SW China. *Earth Planet Sci Lett.* 2014; 339, 21-29. https://doi.org/10.1016/j.epsl.2014.05.002
42. Yoshiya K, Nishizawa M, Sawaki Y, et al. In situ iron isotope analyses of pyrite and organic carbon isotope ratios in the Fortescue Group: Metabolic variations of a Late Archean ecosystem. *Precambrian Res*. 2012;212:169-193. https://doi.org/10.1016/j.precamres.2012.05.003.

43. Nishizawa M, Yamamoto H, Ueno Y, et al. Grain-scale iron isotopic distribution of pyrite from Precambrian shallow marine carbonate revealed by a femtosecond laser ablation multicollector ICP-MS technique: possible proxy for the redox state of ancient seawater. *Geochim Cosmochim Acta*. 2010;74(9):2760-2778. https://doi.org/10.1016/j.gca.2010.02.014.
44. Liu MC, McKeegan KD, Harrison TM, Jarzebinski G, Vltava L. The Hyperion-II radio-frequency oxygen ion source on the UCLA ims1290 ion microprobe: Beam characterization and applications in geochemistry and cosmochemistry. *Int J Mass Spectrom*. 2018;424:1-9. https://doi.org/10.1016/j.ijms.2017.11.007.
45. Fukuda K, Beard BL, Dunlap DR, et al. Magnesium isotope analysis of olivine and pyroxene by SIMS: Evaluation of matrix effects. *Chem Geol*. 2020;119482. https://doi.org/10.1016/j.chemgeo.2020.119482.
46. Villeneuve J, Chaussidon M, Marrocchi Y, Deng Z, Watson EB. High-precision in situ silicon isotopic analyses by multi-collector secondary ion mass spectrometry in olivine and low-calcium pyroxene. *Rapid Commun Mass Spectrom*. 2019;33(20):1589-1597. https://doi.org/10.1002/rcm.8508.
47. Ushikubo T, Nakashima D, Kimura M, Tenner TJ, Kita NT. Contemporaneous formation of chondrules in distinct oxygen isotope reservoirs. *Geochim Cosmochim Acta*. 2013;109, 280-295. https://doi.org/10.1016/j.gca.2013.01.045.
48. Marin-Carbonne J, Rollion-Bard C, Luais B. In-situ measurements of iron isotopes by SIMS: MC-ICP-MS intercalibration and application to a magnetite crystal from the Gunflint chert. *Chem Geol*. 2011;285(14):50-61. https://doi.org/10.1016/j.chemgeo.2011.02.019.
49. Whitehouse MJ, Fedo CM. Microscale heterogeneity of Fe isotopes in > 3.71 Ga banded iron formation from the Isua Greenstone Belt, southwest Greenland. *Geology*. 2007;35(8):719-722. https://doi.org/10.1130/G23582A.1.
50. Muller É, Philippot P, Rollion-Bard C, et al. Primary sulfur isotope signatures preserved in high-grade Archean barite deposits of the Sargur Group, Dharwar Craton, India. *Precambrian Res*. 2017; 295: 38-47. https://doi.org/10.1016/j.precamres.2017.04.029.
51. Muller É, Philippot P, Rollion-Bard C, Cartigny P. Multiple sulfur-isotope signatures in Archean sulfates and their implications for the chemistry and dynamics of the early atmosphere. *Proc Nat Acad Sci*. 2016; 113(27) : 7432-7437. https://doi.org/10.1073/pnas.1520522113.
52. Kita NT, Ushikubo T, Fu B, Valley JW. High precision SIMS oxygen isotope analysis and the effect of sample topography. *Chem Geol*. 2009;264(1-4):43-57. https://doi.org/10.1016/j.chemgeo.2009.02.012.
53. Bayliss P. Crystal structure refinement of a weakly anisotropic pyrite. *Am Mine.* 1977; 62(11-12): 1168-1172.
54. Prior DJ, Boyle AP, Brenker F, et al. The application of electron backscatter diffraction and orientation contrast imaging in the SEM to textural problems in rocks. *Am Mine*. 1999; 84: 1741-1759. https://doi.org/10.2138/am-1999-11-1204.

55. Shimizu N, Hart SR. Applications of the ion microprobe to geochemistry and cosmochemistry. *Annu Rev Earth Planet Sci*. 1982;10(1):483-526.
56. Eiler JM, Graham C, Valley JW. SIMS analysis of oxygen isotopes: Matrix effects in complex minerals and glasses. *Chem Geol*. 1997;138(3-4):221-244.
57. Chaussidon M., Albarede F, Sheppard SMF. Sulphur isotope heterogeneity in the mantle from ion microprobe measurements of sulphide inclusions in diamonds. *Nature*. 1987;330(6145):242-244.
58. Kita NT, Huberty JM, Kozdon R, Beard BL, Valley JW. High-precision SIMS oxygen, sulfur and iron stable isotope analyses of geological materials: Accuracy, surface topography and crystal orientation. *Surf Interface Anal.* 2011;43(1-2):427-431. https://doi.org/10.1002/sia.3424.
59. Vielzeuf D, Champenois M, Valley JW, Brunet F, Devidal JL. SIMS analyses of oxygen isotopes: matrix effects in Fe–Mg–Ca garnets. *Chem Geol*. 2005;223(4):208-226. https://doi.org/10.1016/j.chemgeo.2005.07.008.
60. Vho A, Rubatto D, Putlitz B, Bouvier AS. New Reference Materials and Assessment of Matrix Effects for SIMS Measurements of Oxygen Isotopes in Garnet. *Geostand Geoanal Res*. 2020;44:450-471. https://doi.org/10.1111/ggr.12324.
61. Deloule E, Chaussidon M, Allé P. Instrumental limitations for isotope measurements with a Caméca® IMS-3f ion microprobe: Example of H, B, S and Sr. *Chem Geol Isot Geosci Sect*. 1992;101(1–2):187-192.
62. Crossley RJ, Evans KA, Jeon H, Kilburn MR. Insights into sulfur cycling at subduction zones from in-situ isotopic analysis of sulfides in high-pressure serpentinites and 'hybrid'samples from Alpine Corsica. *Chem Geol*. 2018; 493, 359-378. https://doi.org/10.1016/j.chemgeo.2018.06.014.
63. Chaussidon M, Deng Z, Villeneuve J, et al. In situ analysis of non- traditional isotopes by SIMS and LA–MC–ICP–MS: Key aspects and the example of Mg isotopes in olivines and silicate glasses. *Rev Mineral Geochem*. 2017;82(1):127-163. https://doi.org/10.2138/rmg.2017.82.5.
64. Kozdon R, Kita NT, Huberty JM, Fournelle JH, Johnson CA, Valley JW. In situ sulfur isotope analysis of sulfide minerals by SIMS: Precision and accuracy, with application to thermometry of~ 3.5 Ga Pilbara cherts. *Chem Geol*. 2010;275(3-4):243-253. https://doi.org/10.1016/j.chemgeo.2010.05.015.
65. Wingate MTD, Compston W. Crystal orientation effects during ion microprobe U–Pb analysis of baddeleyite. *Chem Geol*. 2000;168(1-2):75-97. https://doi.org/10.1016/S0009-2541(00)00184-4.
66. LaFlamme C, Martin L, Jeon H, et al. In situ multiple sulfur isotope analysis by SIMS of pyrite, chalcopyrite, pyrrhotite, and pentlandite to refine magmatic ore genetic models. *Chem Geol*. 2016; 444: 1-15. https://doi.org/10.1016/j.chemgeo.2016.09.032
67. Gnaser H. Energy and angular distributions of sputtered species. In: *Sputtering by particle bombardment*. Springer, Berlin, Heidelberg. 2007;231-328.
68. Huberty JM, Kita NT, Kozdon R, et al. Crystal orientation effects in δ18O for magnetite and hematite by SIMS. *Chem Geol*. 2010;276(3-4):269-283. https://doi.org/10.1016/j.chemgeo.2010.06.012.

69. Marin-Carbonne J, Busigny V, Miot J, et al. In Situ Fe and S isotope analyses in pyrite from the 3.2 Ga Mendon Formation (Barberton Greenstone Belt, South Africa): Evidence for early microbial iron reduction. *Geobiology*. 2020;18:306-325. https://doi.org/10.1111/gbi.12385.

Table 1 : SIMS settings for each Fe isotopes session at CRPG-IPNT (February 2018, April 2018 and September 2020) and SwissSIMS (July 2019, January 2020, March 2020 and June 2020) using the Hyperion-II source and resulting $^{56}Fe^{+}$ intensities and ion yields measured on Balmat pyrite. Comparison with settings and $^{56}Fe^{+}$ yields measured with the Duoplasmatron[48,49].

THIS STUDY								**PUBLISHED DATA**	
CRPG-IPNT				SwissSIMS				CRPG-IPNT	Nord SIMS
Hyperion-II				Hyperion-II				Duoplasmatron	
Session	Feb.18	Ap.18	Sep.20	Jul.19	Jan.20	Mar.20	Jun.20	Ref. 48	Ref.49
Field Ap. (µm)	2000		2400	2000				2500	3000
Contrast Ap. (µm)	400			400				400	
Max. Area	80		80 *160*	80				80	160
Entrance Slit (µm)	85		61	61				-	60
Energy slit (eV)	50			50				50	60
Slit Mode	Circular			Circular				Circular	
Exit slit	150 µm (slit 3)			150 µm (slit 3)				150 µm (slit 3)	250 µm (slit 2)
MRP	6100		6800	6700-6800				~7000	<6000
Primary Intensity (nA)	3.40	3.70	3.00	3.14	3.05	2.99	2.80	10	10
$^{56}Fe^{+}$ count rate on Balmat (cps)	6.5E+7	7.45E+7	4.70E+7 *1.51E+7*	4.90E+7	4.85E+7	4.46E+7	4.49E+7	~ 1.2E+8	~1.5E+8
$^{56}Fe^{+}$ yield on Balmat (cps/nA)	1.87E+7	2.01E+7	1.56E+7 *5.05E+6*	1.56E+7	1.59E+7	1.49E+7	1.61E+7	~1.2E+7	1.5E+7

Table 2: True $\delta^{56}Fe$ values of the standards (Balmat and SpainCR pyrites) and corresponding IMF during the different sessions at CRPG-IPNT and SwissSIMS and comparison with published IMF obtained with the Duoplasmatron[48]. The true $\delta^{56}Fe$ value of SpainCR standard was determined by MC-ICP-MS at CRPG using the procedure of ref. 41. The reproducibility is reported as 2SD, standard deviation. n= number of analyses; *n.a*= not available data.

INSTRUMENTAL MASS FRACTIONATION $\delta^{56}Fe_{IMF}$ AND REPRODUCIBILITY (2SD, ‰) (#ANALYSIS)									
	CRPG-IPNT Hyperion-II				SwissSIMS Hyperion-II				CRPG-IPNT Duoplasmatron
Session	Feb. 2018	Apr. 2018	Ju. 2018	Sept. 2020	Ju. 2019	Jan. 2020	Mar. 2020	Jun. 2020	ref.48
Balmat Py.	-33.10 ±0.24 (n=33)	-32.47 ±0.26 (n=133)	*n.a*	-31.20 ±0.30 (n=17)	-35.16 ±0.28 (n=41)	-27.23 ±0.35 (n=16)	-32.34 ±0.18 (n=33)	-33.06 ±0.22 (n=185)	-32.00 ±0.20
SpainCR Py.	*n.a*	*n.a*	-33.21 ±0.28 (n=68)	*n.a*	-35.50 ±0.32 (n=2)	*n.a*	*n.a*	*n.a*	*n.a*

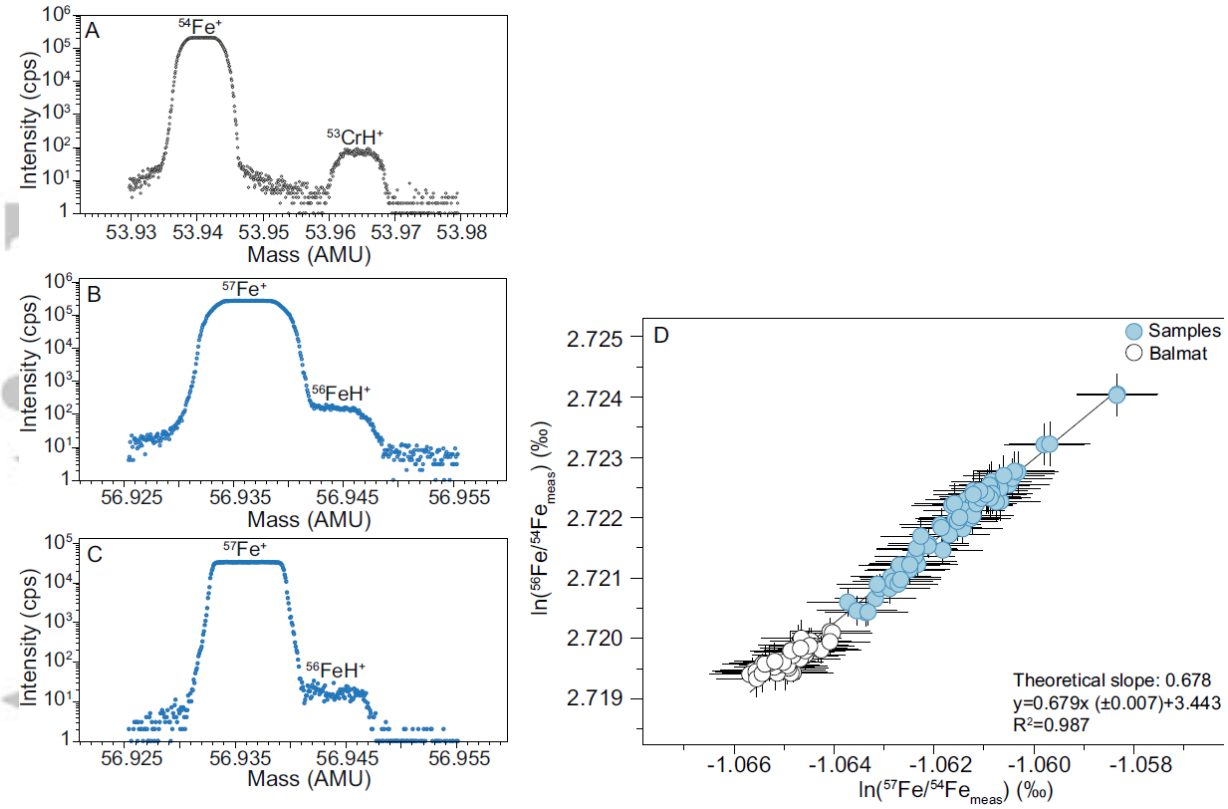

Figure 1 : A) Scan of the 54Fe signal on the axial EM, using a mass resolution of 6800 to reveal the 53CrH+ contribution. This scan was carried out on a Russie magnetite standard which has a detectable Cr content. B) Scan of the 57Fe signal on the axial EM, using a mass resolution of 6800 to reveal the 56FeH+ contribution. C) High mass resolution (MRP 7800) scan of the 57Fe signal, where the 57Fe+ and 56FeH+ peaks are separated. D) Three-isotope plot of the logarithm of the measured Fe isotope ratios in Balmat pyrite standard (white dots) and pyrites from sedimentary rocks (blue dots), corrected for the 54Cr contribution (July 2020 session at SwissSIMS). The regression line gives a slope of 0.679±0.007, which is in good agreement with the theoretical slope of 0.678 within the error bar. The theoretical value represents the mass dependent fractionation law for Fe isotopes using a simple harmonic oscillator approximation. Data are available in Table S1 (supporting information B).

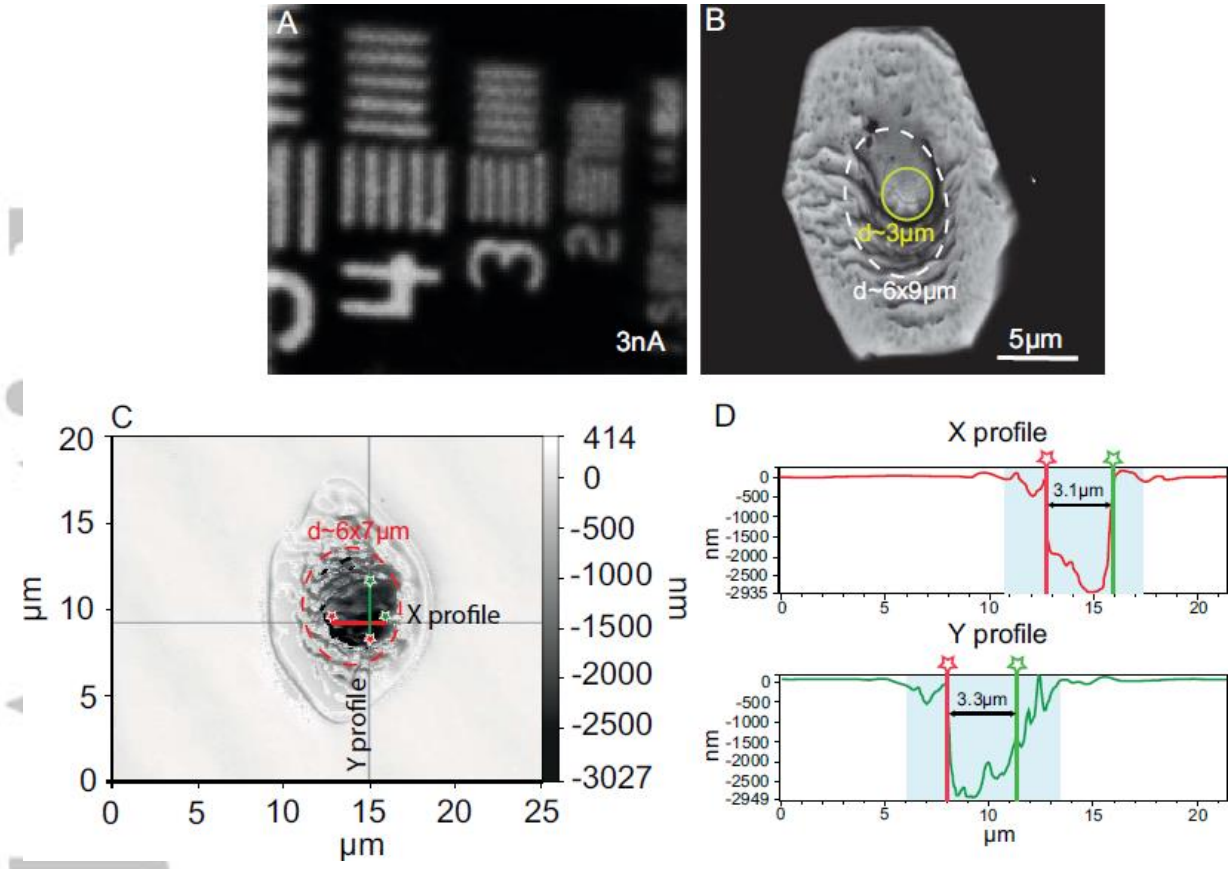

Figure 2 : A) 30Si+ image of the Si-grid on electron multiplier. The spatial resolution of the primary 16Obeam is determined according to the ability to differentiate two silicon bars on the 4µm, 3µm or 2µm grid. B) SEM image of a sedimentary micro-pyrite after SIMS analyses. The shape of the spot is due to the position of the source which makes an angle with the sample surface. C) Image from interferometric microscope of the sputtering pit. D) X and Y topographic profiles measured by interferometric microscope. The profiles refer to the Figure 2C and show the diameter of the pit, which corresponds to the real spot size (measured at the bottom of the pit), and the sputtered area (blue area on Figure 2D and dashed red circle on Figure 2C, measured at the top of the pit).

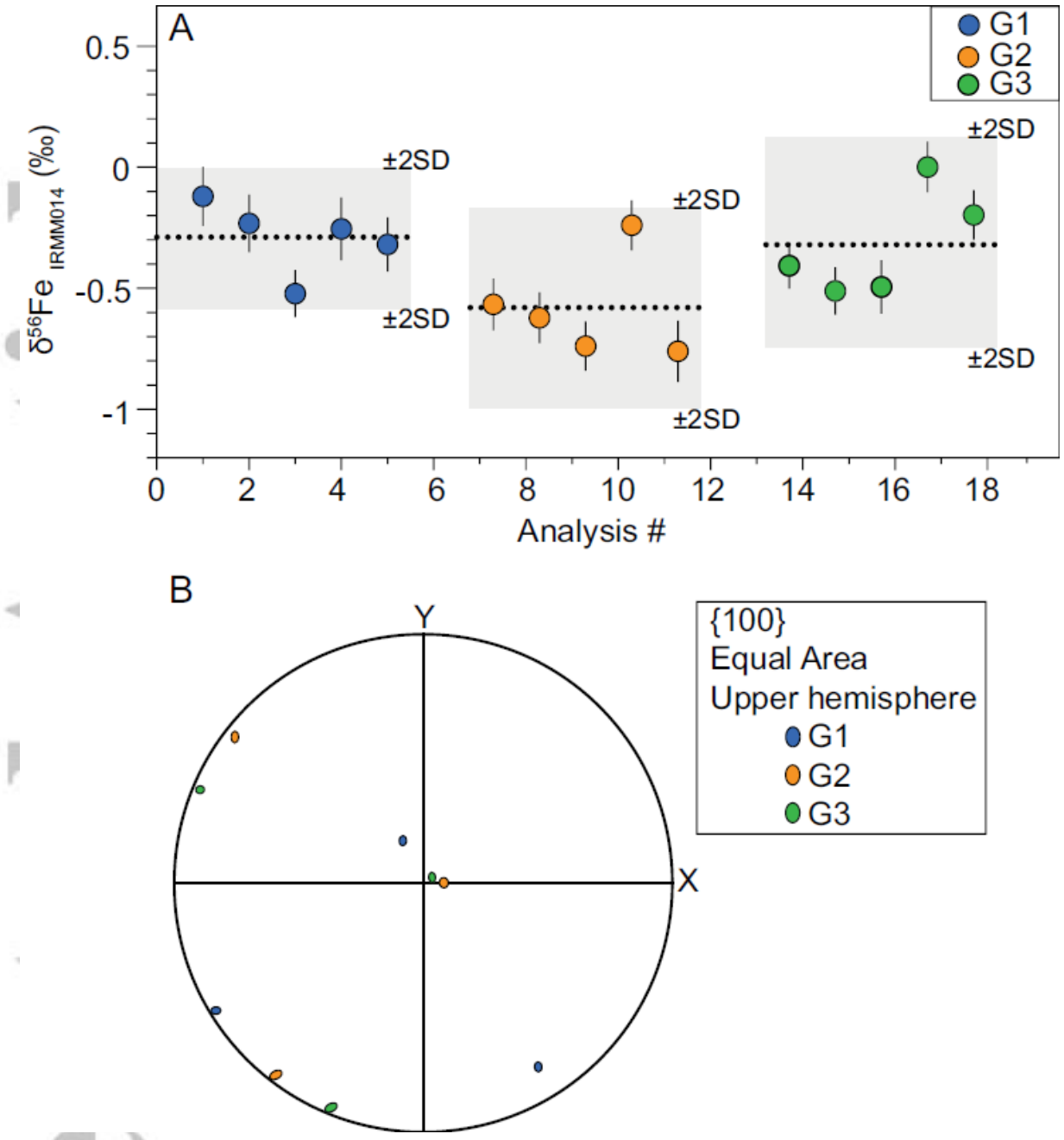

Figure 3 : Crystal orientation (September 2020) test in Balmat pyrite standard. A) δ56Fe corrected from instrumental fractionation measured in three grains prepared in an indium mount. The reproducibilities are given at 2SD and show no clear difference between the grains. Data are available in Table S2 (supporting information). B) Upper hemisphere equal area (i.e. with Z pointing to the reader) EBSD pole figure showing the averaged crystallographic orientations of {100} for the three pyrite grains of interest. Note the strong clustering of [100] axes close to Z.

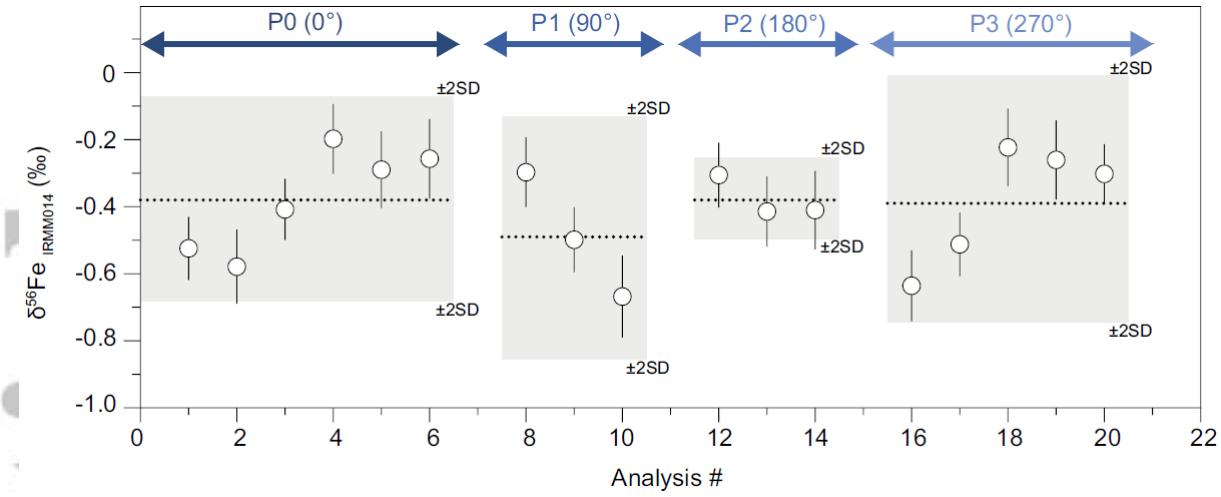

Figure 4 : δ56Fe values IMF-corrected of Balmat pyrite standard rotated by 90° (P1), 180° (P2) and 270° (P3) compared with the initial position (P0). The external reproducibility is ±0.30‰ (2SD) and the internal variabilities are ±0.10‰ to ±0.20‰ (2SE), allowing us to rule out an orientation (channeling) effect on IMF variations. Data are available in Table S2 (supporting information).

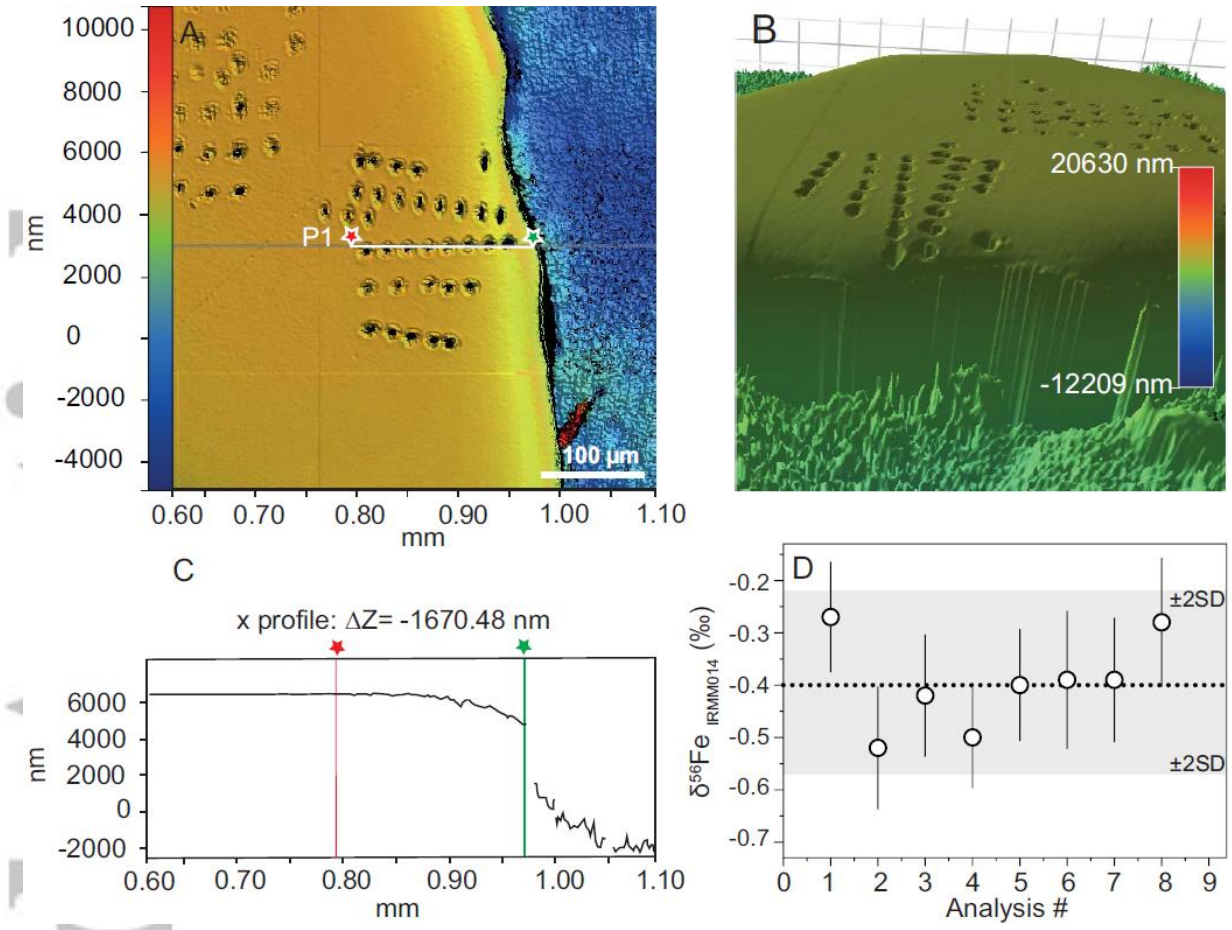

Figure 5: Profile in Balmat reference material. A) Interferometric microscope image showing Pf1 profile in the pyrite grain. B) Interferometric microscope 3D image of the pyrite standard. C) Topographic profile following Pf1 transect. This profile shows a topographic difference of ~1.7µm between the core (red star) and the rim (green star) of the grain. The gap after the green star (~7µm) highlights the boundary between the pyrite grain and the indium. D) δ56Fe values IMF-corrected in a core to rim profile performed in Balmat pyrite standard. Dashed black line is the true δ56Fe value of Balmat standard (δ56Fe= -0.399‰). The uncertainty on average is ±0.09‰ (2SE) and the external reproducibility is ±0.18‰ (2SD, grey area). Data are available in Table S2 (supporting information).

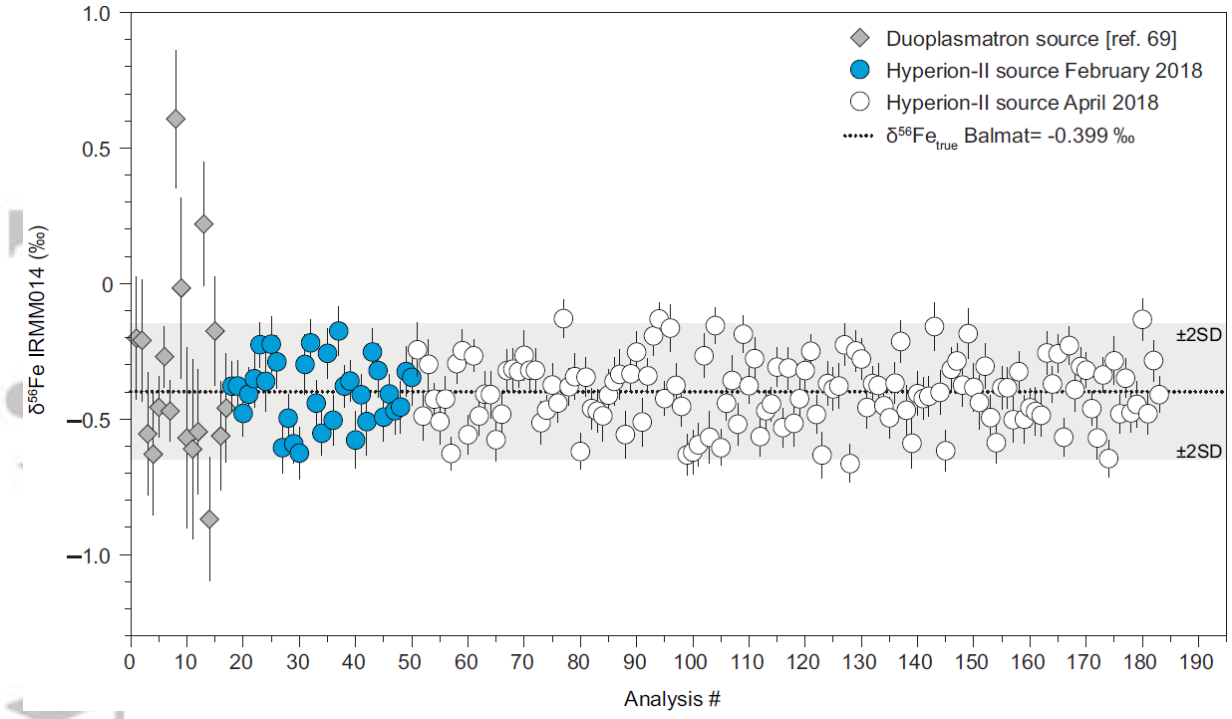

Figure 6: Long-term reproducibility on Balmat pyrite reference material (0.25‰, 2SD). Dots are δ56Fe measured with Hyperion-II Radio-Frequency plasma source in February 2018 (blue dots) and April 2018 (white dots) session. Grey diamonds are δ56Fe data from Duoplasmatron source (reference 69). Dash black line indicates the true δ56Fe value for Balmat (δ56Fe= -0.399‰) and grey area represents the long-term reproducibility of ±0.25 at 2SD, standard deviation. February 2018 data are available in Table S3 (supporting information B).